Article

Single-Crystal Growth of a Cubic Laves-Phase Ferromagnet HoAl$_2$ by a Laser Floating-Zone Method

Naoki Kikugawa [1,*], Takashi Kato [2,3], Momoko Hayashi [2] and Hitoshi Yamaguchi [2]

[1]   National Institute for Materials Science, Tsukuba 305-0003, Ibaraki, Japan
[2]   National Institute for Materials Science, Tsukuba 305-0047, Ibaraki, Japan; katou@fukushima-nct.ac.jp (T.K.); hayashi.momoko@nims.go.jp (M.H.); yamaguchi.hitoshi@nims.go.jp (H.Y.)
[3]   National Institute of Technology, Fukushima College, Iwaki 970-8034, Fukushima, Japan
[*]   Correspondence: kikugawa.naoki@nims.go.jp

Abstract: The successful growth of single crystals of a cubic Laves-phase material HoAl$_2$ with the space group *Fd-3m* is reported in this study. The crystals were grown by a floating-zone method with five laser diodes as a heat source. Al-rich feed rods were prepared as compensation for heavy evaporation during the growth. The nominal ratio for the feed rods was optimized as Ho:Al = 1:2.5. Single crystals of HoAl$_2$ with a length of 50 mm were first grown in this technique. Obtaining the large-sized crystal by the floating-zone method enabled us to systematically explore the physical properties using the same batch crystal. The crystal possessed a second-ordered ferromagnetic transition at 29 K and a first-ordered spin-reorientation transition at 20 K. The bulk physical properties, such as specific heat, magnetic susceptibility, isothermal magnetization, and thermal expansion measurements, were measured. Additionally, a magnetocaloric effect was evaluated by the magnetic entropy change. We demonstrate that anisotropic physical properties along the principal axes ([100], [110], and [111]) emerged below the magnetically ordered states, in contrast to the isotropic behavior in the paramagnetic state.

Keywords: HoAl$_2$; crystal growth; laser floating-zone technique; bulk physical properties; magnetocaloric effect

1. Introduction

The magnetocaloric effect is a thermodynamic phenomenon of temperature change on a magnetic material controlled by an external magnetic field in adiabatic conditions [1,2]. Magnetic refrigeration is a promising application based on the magnetocaloric effect because of its potential for being environmentally friendly and highly efficient [3]. The material design exhibiting an efficient magnetocaloric effect has been a central key to the practical use of magnetic refrigeration. One of the efficiencies of the magnetocaloric effect can be assessed by the magnetic entropy change in the material, defined as the difference in entropy between the magnetized and demagnetized process. Ferromagnetic materials have usually been targeted because these materials should generally gain larger magnetic entropy change between the demagnetized (higher entropy) and magnetized (lower entropy) process near the transition temperature [4]. As the transition temperature widely varies from material to material, we can focus on the design of the material by demonstrating the excellent magnetocaloric effect at the focused temperature. Among the target temperature ranging from room temperature for air conditioners to extremely low temperatures, one of the focused temperatures is approximately 20 K which liquefies hydrogen as a next-generation clean-energy source [5,6].

Very recently, an active magnetic regenerative refrigerator combined with a superconducting magnet has been developed and succeeded in liquefying hydrogen [7]. This opens a new window to hydrogen liquefaction through the novel magnetic refrigeration technique in addition to the conventional gas compression/expansion technique. Here,

HoAl$_2$ was selected as a magnetic refrigerant among the materials because this material has a large magnetic entropy change around the temperature for hydrogen liquefaction.

HoAl$_2$ has the cubic Laves-phase structure with the space group *Fd-3m* (No. 227) [8]. The crystal structure is illustrated in Figure 1. HoAl$_2$ exhibits a ferromagnetic transition around 30 K as well as another spin-reorientation transition at 20 K [9]. For the above magnetic refrigeration, the HoAl$_2$ polycrystalline material with a total weight of 250 g was filled inside the refrigerator as stamped particles with a diameter of 300–500 μm [7]. Additionally, a gas-atomization process was applied to make spherical polycrystalline particles with a diameter of 200–400 μm [10]. Producing many particles with homogeneous quality is one of the important factors for efficient liquefaction. Since the quality of the produced particles is directly linked to the liquefaction efficiency, it is useful to assess the variation in quality based on a "standard dataset" obtained from the reference material, preferably high-quality single crystals of HoAl$_2$. In addition, the materials are exposed to both the cryogenic cycle and the application/removal of the magnetic fields during the liquefaction [7,11]. Since the crystalline material generally has anisotropic physical properties such as thermal contraction/expansion and magnetostriction, these may affect the sample durability under these extreme circumstances. Acquiring the anisotropic physical properties is an important task, and the investigation using a single crystal is in high demand.
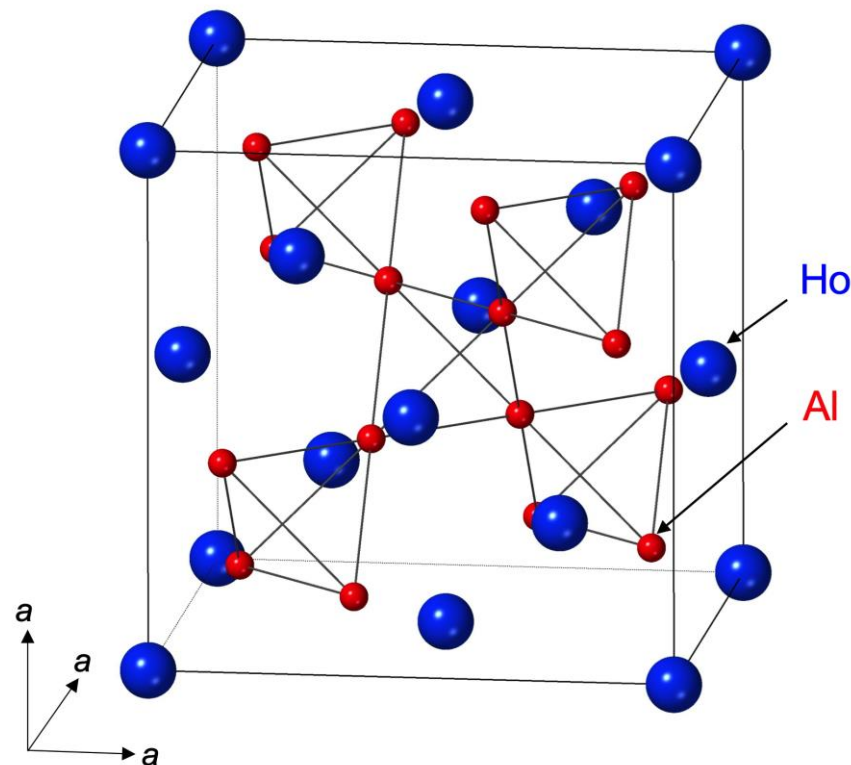

Figure 1. Crystal structure of a cubic Laves-phase material HoAl$_2$ with the space group *Fd-3m* (No. 227).

Physical properties of the single-crystalline HoAl$_2$ grown by the Czochralski and Bridgman methods have been presented both experimentally and theoretically [9,12–16]. However, to our knowledge, crystal growth with a floating-zone technique has not been reported. An advantage of the floating-zone method is minimized contamination level during the growth procedure due to the absence of the crucible, as well as the possibility to obtain large and homogeneous crystals [17]. These enable us to perform characterization by several experimental techniques using the same batch of grown crystals. In this paper, we first present the successful growth of HoAl$_2$ crystals by the floating-zone technique with five laser diodes as the heat source [18,19]. Although we found that the procedure for the growth process of another intermetallic system NdAlGe [20] was partly applicable to the growth of HoAl$_2$, we mention improved steps, such as the fabrication of Al-rich feed

rods to compensate for the heavy evaporation during the growth of $HoAl_2$. We show the thermodynamic physical properties such as specific heat, magnetic susceptibility, magnetization, and thermal expansion of the grown crystals. Throughout the measurements, the anisotropic physical properties are revealed in the ferromagnetic ordered state along the principal axes, in sharp contrast to the isotropic behavior in the paramagnetic state.

2. Materials and Methods

2.1. Growth by the Floating-Zone Technique

We employed a floating-zone technique using a laser diode as the heat source (L-FZ 2000, Quantum Design Japan, Tokyo, Japan) with five 400 W GaAs-based 940 nm laser heads for the growth of $HoAl_2$ single crystals. Since the laser emission can be sharply focused, a steep temperature gradient can be created between the laser-heated narrower molten zone and the grown crystal. That provides a stable molten zone during crystal growth. Additionally, we optimized the distribution profile of the vertical irradiation intensity along the length of the rod, improving from a "flat" to a "bell-shaped" form, while the original flat temperature profile was kept along the radial direction of the rod (see Figure 2 of [19]). Such a modified profile reduces thermal stress inside the grown crystals. $HoAl_2$ single crystals were grown using a laser-diode floating-zone furnace where five laser diodes provide the mentioned vertically bell-shaped distribution of temperature at the focal point.

2.2. Feed and Seed Rods Preparation

When we first attempted the crystal growth of $HoAl_2$ using the feed rod with the nominal stoichiometric ratio Ho:Al = 1:2, the molten zone was stable during the growth process. However, we found high volatility from the feed rods, and the evaporated powder was deposited inside the quartz tube. The grown bulk crystal finally collapsed into powder when it was left in the air overnight. The collapsed powder was composed of Ho_2O_3, and HoN after probably absorbing the air, together with $HoAl_2$ as the main phase by the X-ray diffraction measurements. Additionally, the evaporated powder was identified as aluminum. To grow the stoichiometric crystals, we made the Al-rich feed rods. The nominal ratio was finally optimized as Ho:Al = 1:2.5 to compensate for the Al evaporation during the growth. We denote the feed rod as $HoAl_{2.5}$ hereafter. For making a feed rod, polycrystalline ingots of $HoAl_{2.5}$ were first prepared using an arc-melting furnace under an Ar atmosphere (Techno Search Corp., Model SE-11399, Tokyo, Japan) with Ho (3N) and Al (5N) as starting materials. The ingot with a button shape was inverted and melted several times to ensure homogeneity. No weight loss by evaporation was detected at this stage. Next, the ingots with a typical weight of 15 g were powdered using an agate mortar and pestle. We shaped the powder into a cylindrical rod in a tubular rubber balloon and then applied hydrostatic pressure of 40 MPa for 5 min. The uniformly shaped rods removed from the balloon were sintered for 24 h at 1123 K in a tube furnace under flowing Ar gas at 3 L/min. Here, the Ar gas was circulated by using a yttria-stabilized zirconia-based oxygen pump heated at 873 K. The oxygen pump produced an extremely low oxygen partial pressure below 10^{-28} atm (Canon Machinery Inc., Model ULOCE-530, Shiga, Japan) [21]. Finally, the sintered rod with typically 5.5 mm diameter was cut into two unequal parts. The longer (shorter) parts 95 mm (30 mm) in length were designated as the feed (seed) rods. Based on the experience of working in ruthenates [22], great care was taken in all the preparation steps to prevent contamination risk.

2.3. Crystal Growth

The sintered feed rod ($HoAl_{2.5}$) was attached to a platinum hock in the upper shaft with a molybdenum wire, and the seed rod was mounted on an alumina holder in the lower shaft. As the growth space was isolated from the outside environment by a quartz tube, the desired gas atmosphere and pressure were selected throughout the crystal growth. For the $HoAl_2$ growth, a gas mixture of Ar (96%) and H_2 (4%) was used for reduction.

An additional thinner quartz tube of smaller diameter was installed inside the main tube to prevent damage to the outer tube by evaporating Al. The melting started from the bottom edge of the feed rod with increasing laser power. Then, the molten feed rod was attached to the upper end of the seed rod. The growth began with necking twice to ensure high crystallinity as a polycrystalline seed rod was used. The molten zone was stabilized at both feed and growth speeds of 5 mm/h after the second necking. The growth was performed at 0.3 MPa under a flow rate of 1 L/min to suppress the evaporation. To grow under homogenized molten liquid and temperature distribution, the feed and seed were rotated at 10 rpm in opposite directions. A stable molten zone was formed during the growth process until the end without cracks in the sintered feed rods prepared using the given procedure. After growth, the crystal was carefully removed from the furnace. The crystal grown using the $HoAl_{2.5}$ rod was kept in bulk without collapsing to powder after the crystal was left in the air. We observed successful growth using a feed rod with the nominal ratio of Ho:Al = 1:2.2, and the crystal did not collapse under air. However, the grown crystal from the $HoAl_{2.2}$ rod was still off-stoichiometry, suggesting Al deficiency, as described later.

2.4. Characterization

To check the phase purity, the ground single crystals were measured with powder X-ray diffraction using Cu *Kα* radiation at room temperature (MiniFlex600, Rigaku, Tokyo, Japan). The grown crystals were cut along the principle crystallographic axes ([100], [110], and [111] directions) by determining their orientations using a back-scattered X-ray Laue diffraction technique (SA-HF3S, Rigaku Co., Ltd., Tokyo, Japan, and s-Laue, Pulstec Industrial Co., Ltd., Shizuoka, Japan). The chemical composition of the grown crystals was analyzed using inductively coupled plasma optical emission spectrometry (ICP-OES).

Thermodynamically bulk physical properties of the grown crystals were measured down to 2 K using a Physical Property Measurement System (Dynacool, Quantum Design). The specific heat (C_P) as a function of temperature (T) was performed by a relaxation method. The magnetic susceptibility between 2 and 300 K was measured in a magnetic field (H) of 0.01 T under both zero-field-cooled (ZFC) and field-cooled (FC) conditions. Here, the ZFC and FC refer to cooling conditions before and after applying a static magnetic field to the sample, respectively. The isothermal magnetization (M) at various temperatures was measured up to 9 T. The thermal expansion was performed by a capacitive-based method [23] with decreasing temperature at the control of 0.1 K/min. The magnetic entropy change (ΔS_M) along the magnetic field directions of [100], [110], and [111] was deduced from the thermodynamic Maxwell relation, $\Delta S_M = \int_0^H \frac{\partial M}{\partial T} dH$ [4], which was obtained from the magnetization (M) measurement as a function of temperature measured up to 5 T under the FC process.

3. Results and Discussion

3.1. Growth of $HoAl_2$ Crystals

A photograph of the $HoAl_2$ crystal with a length of 50 mm grown under stable conditions is demonstrated in Figure 2a. The evaporated Al powder from the rod was deposited on the internal surface of the quartz tube and the shafts. No sign of the molten liquid dropping during the growth was spotted on the crystal surface, indicating stable temperature control. Figure 3 presents the powder X-ray diffraction profile of a partially crushed crystal. For comparison, an X-ray diffraction profile of $HoAl_2$ from a database (PDF-2 03-065-7339 (ICDD, 2021)) [24] is added with red color. All peaks were sharp and well indexed to the *Fd-3m* space group without detecting impurity phases. The lattice parameters were deduced to be a = 0.7838 nm, which was consistent with the previous report [25]. The back-scattered Laue photos of the crystal along the axes [100], [110], and [111] after polishing are presented in Figure 2b–d, respectively, with sharp and clear spots from the bulk crystal. We can clearly see the four-, two-, and three-fold symmetry in the photos of [100], [110], and [111], respectively, reflecting the crystal symmetry of the cubic

structure (*Fd-3m*). ICP-OES suggests the molar ratios of Ho:Al = 1.00:1.97, and 1.00:2.00 in the grown crystals for the $HoAl_{2.2}$ and $HoAl_{2.5}$ nominal compositions of the feed rods, respectively. Each ratio was identical to the different positions of the grown crystal within the experimental error, indicating the homogeneity of the grown crystal. This certifies that the stoichiometric crystal was grown from the $HoAl_{2.5}$ feed rod where excess Al compensated for the evaporation, whereas the crystal grown from the $HoAl_{2.2}$ feed rod still had Al deficiency. The possibility of Al embedding into the grown crystals when using off-stoichiometric (Al-rich) feed rods had to be verified following our experience in growing Ru-embedded Sr_2RuO_4 [26]. Any signals of quantum oscillatory effects originating from aluminum were not detected within the experimental resolution when the measured AC susceptibility of the grown material was at 30 mK. Since the AC susceptibility measurement using a field modulation technique [27] is a powerful tool that can detect the micrometer-size metal inclusions inside the bulk material, our results strongly suggest that there is no effect of Al embedding on the bulk physical properties of $HoAl_2$. Hereafter, we show the bulk physical properties of the stoichiometric crystal $HoAl_2$ (grown from the feed rod of $HoAl_{2.5}$). Here, the thermodynamic physical properties in bulk were measured with dimensions of 2.0 mm and a weight of 47 mg after cutting and polishing along the principal axes ([100], [110], and [111]), as shown in Figure 2e. Appendix A shows the sample dependence between $HoAl_2$ and $HoAl_{1.97}$ found in the specific heat measurements.
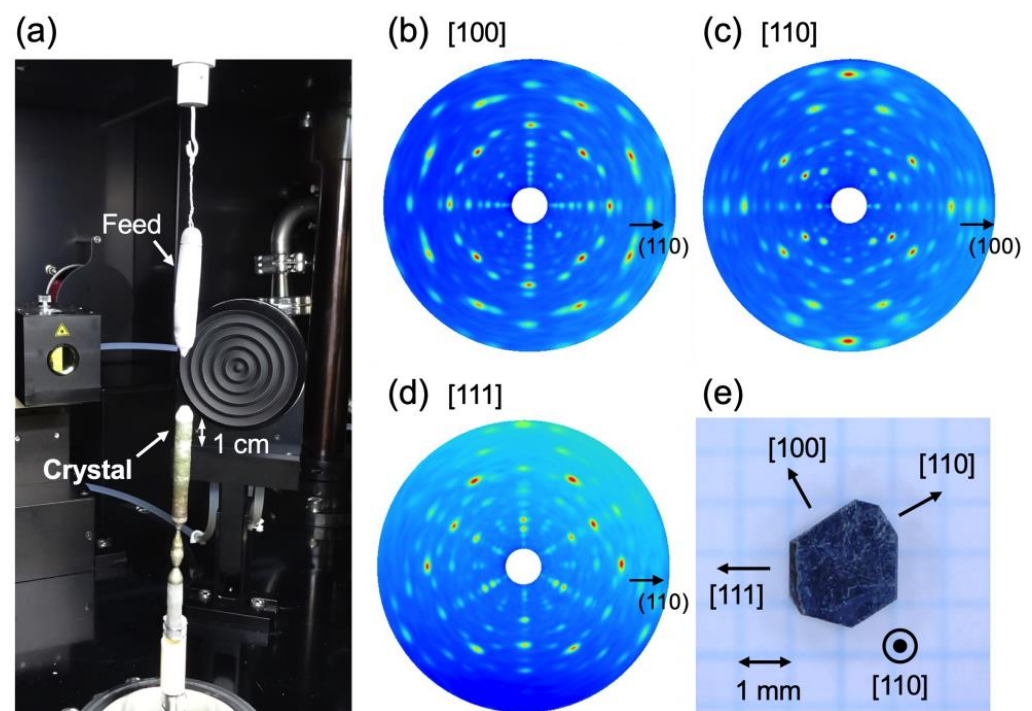

Figure 2. (**a**) A photograph of the grown $HoAl_2$ crystal after the floating-zone method using five laser diodes as the heat source. The crystal was obtained after necking twice at the beginning of the growth. (**b**–**d**) Back-scattered Laue photos along the principal axes [100], [110], and [111], respectively. (**e**) A photograph of the $HoAl_2$ crystal after cutting and polishing along the principal axes for the measurements of the thermodynamic physical properties used in this study.
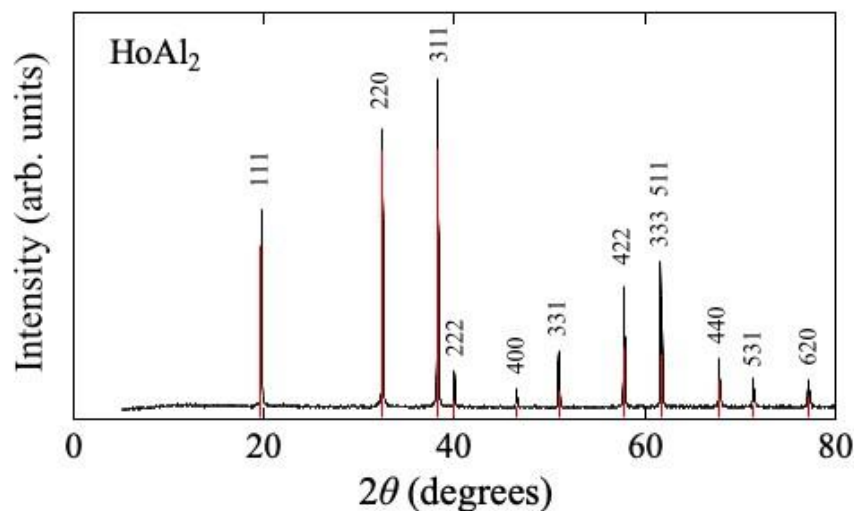
Figure 3. Powder X-ray diffraction pattern with indices of the partially crushed $HoAl_2$ crystal using Cu *Kα* radiation at room temperature. For comparison, an X-ray diffraction profile of $HoAl_2$ from a database (PDF-2 03-065-7339 (ICDD, 2021)) [24] is added with red color.

3.2. Bulk Thermodynamic Properties of the Grown Crystal

In Figure 4, the temperature dependence of the specific heat (C_P) for the stoichiometric $HoAl_2$ without field represents a clear lambda-type anomaly with a second-ordered transition temperature at 29 K defined by the midpoint of the jump. The transition corresponds well to the onset of the ferromagnetic transition at T_C from the paramagnetic state. Another sharp transition was seen at 20 K (T_{SR}), defined at the peak, which corresponds to a first-ordered spin-reorientation transition [9]. The results certify that the observed phase transitions occur in bulk. No other transitions from impurity phases were detected in our experimental resolution down to 2 K except for these two sharp ones. For comparison, the C_P of Al-deficient $HoAl_{1.97}$ crystal is shown in Appendix A (Figure A1). We can see that the T_C of $HoAl_{1.97}$ is lower than that of the stoichiometric $HoAl_2$. On the other hand, T_{SR} seems almost identical. It should be noted that we were careful about evaluating the specific heat value for the first-ordered transition when the relaxation method is applied.
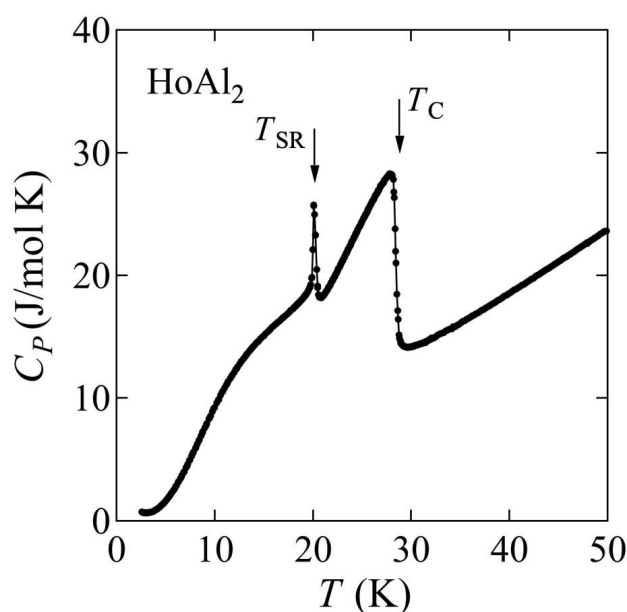

Figure 4. Temperature dependence of specific heat (C_P) of $HoAl_2$ crystal under zero field. Clear transitions with a second-ordered and a first-ordered feature are seen at T_C = 29 K and T_{SR} = 20 K, respectively.

In Figure 5a–c, temperature dependences of the magnetic susceptibility (M/H) were presented under the applied magnetic field of 0.01 T under $H//[100]$, [110], and [111], respectively. A clear ferromagnetic transition (T_C) at 29 K as well as the spin-reorientation transition at 20 K (T_{SR}) was seen in all field directions. Both T_C and T_{SR} correspond to the transitions seen at the specific heat in Figure 4. The hysteresis between ZFC and FC process is clearly observed below T_{SR} as demonstrated in the inset of Figure 5b. The inverse magnetic susceptibility $(M/H)^{-1}$ as a function of temperature along the field directions [100], [110], and [111] in Figure 5d–f, respectively, involves the black lines, which represent the fits to the Curie–Weiss law, $\frac{M}{H} = \frac{N_A \mu_{eff}^2 \mu_B^2}{3 k_B (T - \theta_P)} + \chi_0$. Here, k_B, N_A, and μ_B are the Boltzmann constant, Avogadro's number, and the Bohr magneton, respectively. The effective magnetic moments (μ_{eff}) determined from the fits between 110 and 300 K were μ_{eff} = 11.1 μ_B, 11.0 μ_B, and 11.2 μ_B under $H//[100]$, [110], and [111], respectively. These values match with the theoretical value of the free Ho^{3+} with a total angular momentum of $J = 8$, which corresponds to μ_{eff} = 10.6 μ_B. This suggests that the nature of the 4f electrons is well localized. The χ_0 is a small temperature-independent term and typically represents Larmor diamagnetic and Pauli paramagnetic contributions. The values from the fits were $+7.65 \times 10^{-4}$, $+6.20 \times 10^{-4}$, and $+5.87 \times 10^{-4}$ emu/mol for H//[100], [110], and [111], respectively. The Weiss temperatures under $H//[100]$, [110], and [111] were obtained as θ_P = +34.6 K, +33.4 K, and +36.1 K, respectively. The positive values of θ_P indicate a ferromagnetic coupling. Thus, the magnetic susceptibility measurements reveal almost isotropic behavior in the paramagnetic region, as found in the previous result that reports only under $H//[100]$ and [110] [15].
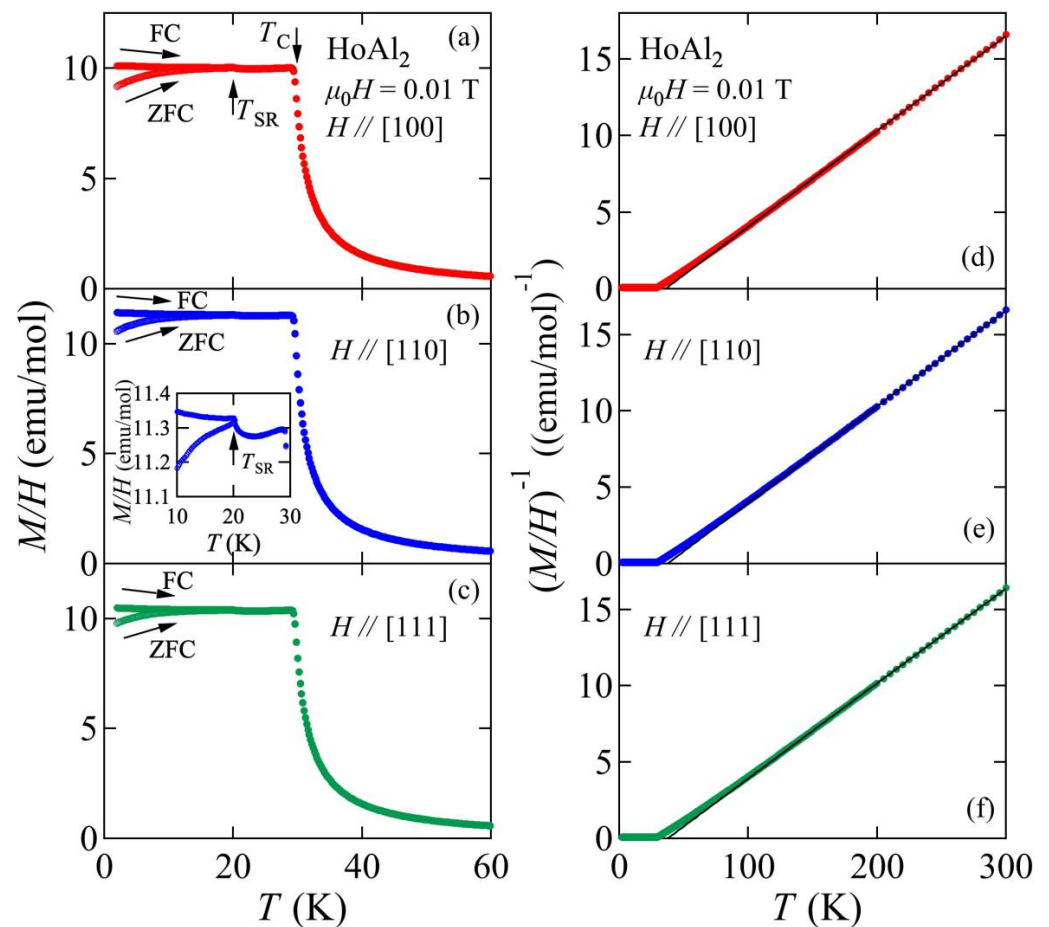

Figure 5. Temperature dependencies of the magnetic susceptibility (M/H) of HoAl$_2$ under the applied field along (**a**) $H//[100]$, (**b**) $H//[110]$, and (**c**) $H//[111]$. Measurements were performed at 0.01 T under

zero-field-cooled (open circles) and field-cooled (closed circles) processes. The inset shows the hysteresis between ZFC and FC processes. Inverse magnetic susceptibility, $(M/H)^{-1}$, as a function of temperature under (**d**) $H//[100]$, (**e**) $H//[110]$, and (**f**) $H//[111]$. Solid black lines represent fits to the Curie–Weiss law between 110 and 300 K.

The isothermal magnetization of HoAl$_2$ under $H//[100]$, [110], and [111] at several temperatures between 2 and 50 K in Figure 6a–c, respectively, was taken after the field cooling process. The rapid increase at lower fields was gradually suppressed under any field directions as the temperature increased. Under $H//[100]$, the upward behavior around 2 T observed at low temperatures was suppressed with increasing temperature. At a high field, the magnetization is saturated toward the full moment (10 μ_B), which corresponds to a free Ho^{3+} ($J = 8$) with the g-factor $g_J = 5/4$, irrespective of the field directions. The remnant magnetization that was seen under all the field directions disappears at T_C.
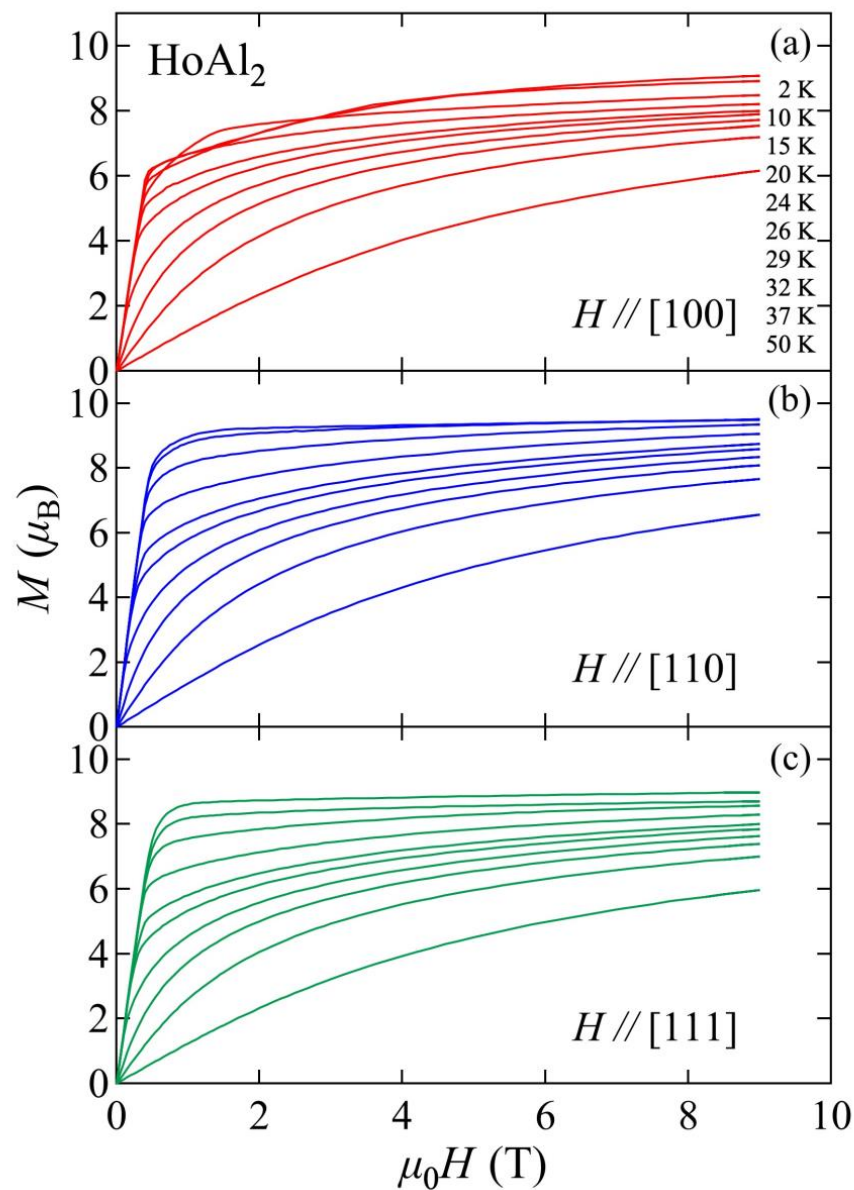

Figure 6. Isothermal magnetization (*M*) of HoAl$_2$ under (**a**) $H//[100]$, (**b**) $H//[110]$, and (**c**) $H//[111]$ up to 9 T at several temperatures across the magnetic phase transitions (T_C and T_{SR}). The data were taken under the field-cooled processes at 2, 10, 15, 20, 24, 26, 29, 32, 37 and 50 K.

In Figure 7, the linear thermal expansions $\frac{\Delta L_i}{L_i} = \frac{L_i(T)-L_i(300\ \mathrm{K})}{L_i(300\ \mathrm{K})}$ as a function of temperature, where the index i refers to the principal crystallographic axes (100), (110), and (111), represent a clear kink at T_C = 29 K for all $\frac{\Delta L_i}{L_i}$, corresponding to the second-ordered ferromagnetic transition. In addition, a jump is seen at T_{SR} = 20 K, indicating the first-ordered transition associated with the spin reorientation. As shown in the inset of Figure 7, the $\frac{\Delta L_i}{L_i}$ is almost isotropic at the paramagnetic region. In contrast, we can see the anisotropic behavior below T_C: on cooling, the $\frac{\Delta L_i}{L_i}$ decreases along all the directions with the largest response to the (110) direction. Additionally, the $\frac{\Delta L_i}{L_i}$ along the (100) and (111) directions decrease suddenly at T_{SR}, whereas the $\frac{\Delta L_i}{L_i}$ along the (110) direction increases. This result may be related to the spin-reorientation transition toward the (110) direction. Thus, the thermal expansion experiments offer directionally bulk information along the independent crystallographic axes throughout the magneto-volume coupling in the magnetically ordered phase.
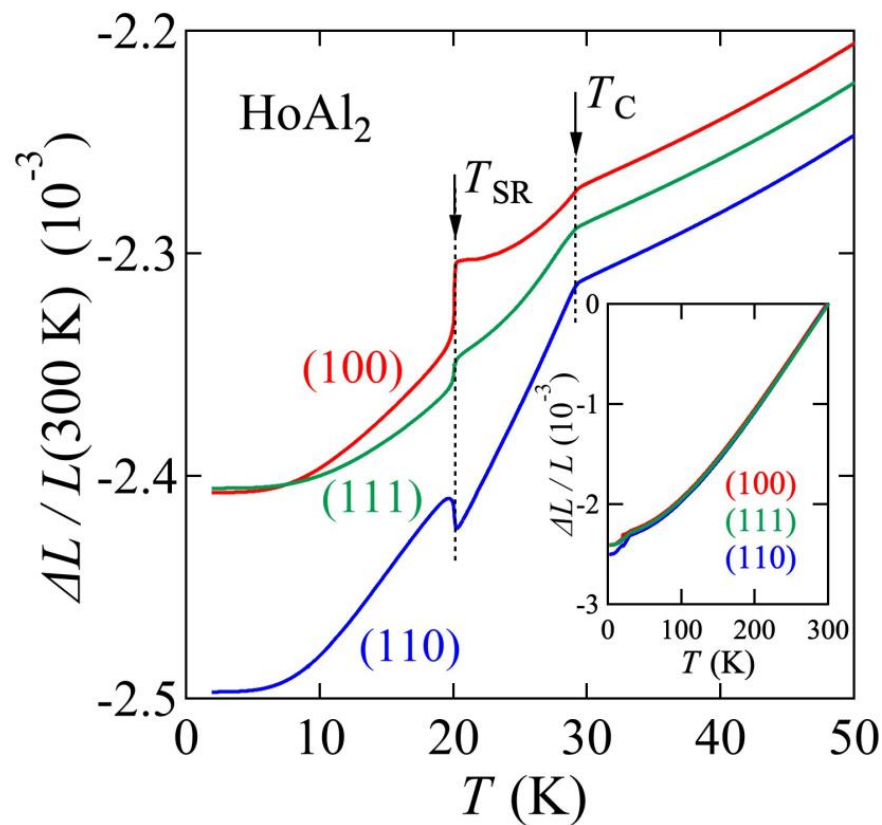

Figure 7. Temperature dependences of thermal expansion $\frac{\Delta L_i}{L_i} = \frac{L_i(T)-L_i(300\ \mathrm{K})}{L_i(300\ \mathrm{K})}$. Here, the index i refers to the principal crystallographic axes [100], [110], and [111], respectively.

To evaluate the magnetic entropy change ΔS_M of single-crystalline $HoAl_2$, the temperature dependences of the magnetization (M vs. T) of $HoAl_2$ under $H//[100]$, [110], and [111] under various static magnetic fields up to 5 T were plotted in Figure 8a–c, respectively. These were measured under the FC process. The Maxwell relation as mentioned above was applied to evaluate the magnetic entropy change ΔS_M. The ΔS_M as the functions of temperature under $H//[100]$, [110], and [111] are shown in Figure 8d–f, respectively, for various applied fields up to 5 T. The ΔS_M has a minimum near T_C for all the field directions. The minimum values obtained for a field change between 0 and 5 T are −5.9, −5.8, and −4.9 J/K mol under $H//[100]$, [110], and [111], respectively. These negative ΔS_M with relatively large values around 30 K indicates the entropy release (gain) under magnetization (demagnetization) independent of the magnetic field directions. This result

of being nearly field-independent might be advantageous as a magnetic refrigerant where polycrystalline particles are used [7,10]. Additionally, under $H//[110]$ and [111], a convex (concave) upward behavior was seen around 20 K, although overall ΔS_M behavior became negative. The ΔS_M under $H//[100]$ showed a positive peak at low temperatures as well as a negative peak around 30 K. Similar sign change can be seen in the previous report [15]. The anisotropic behavior around 20 K might be associated with the spin-reorientation transition. These results indicate that the main contribution in ΔS_M originates from the paramagnetic to the ferromagnetic transition at T_C irrespective of the field directions, and the spin orientation transition induces the anisotropic behavior in ΔS_M.

Figure 8. Temperature dependence of magnetization of HoAl$_2$ under (**a**) $H//[100]$, (**b**) $H//[110]$, and (**c**) $H//[111]$. The applied magnetic fields are 0.01, 0.1, 0.3, 0.5, 0.7, 1, 2, 3, 4, and 5 T. The data were taken under field-cooled processes. The magnetic entropy change ΔS_M as a function of temperature under (**d**) $H//[100]$, (**e**) $H//[110]$, and (**f**) $H//[111]$.

4. Summary

Single crystals of a cubic Laves-phase ferromagnet $HoAl_2$ were successfully grown by the laser diode-based floating-zone method. Here, the laser diodes as the heat source provided the vertically bell-shaped distribution of temperature at the focal point. Since Al evaporation was inevitable during the growth, we prepared Al-rich feed rods to compensate for the evaporation. The nominal ratio was optimized as Ho:Al = 1:2.5 to grow the stoichiometric crystals. Finally, a large-size crystal with a 50 mm length was obtained under stable conditions.

The crystal exhibited a second-ordered ferromagnetic transition at T_C = 29 K and a first-ordered spin-reorientation transition at T_{SR} = 20 K. These transitions occurred in bulk. The isothermal magnetization showed a typical ferromagnetic behavior along the field directions [110] and [111]. For the magnetization under $H//$[100], the upward behavior around 2 T observed at low temperatures was suppressed with increasing temperature. The magnetic entropy changes under the applied field along the principal axes had a relatively similar minimum value around T_C, and the anisotropy became obvious at lower temperatures. In particular, the magnetic entropy change under $H//$[100] showed a positive peak at lower temperatures. The linear thermal expansion measurements to detect the directional information also revealed an anisotropic behavior below T_C. The anisotropic behavior in the ordered state is in sharp contrast to the almost isotropic behavior shown in the paramagnetic region beyond T_C. We emphasize that the floating-zone technique is useful for the crystal growth of intermetallic alloys because this method enables us to systematically investigate the fundamental properties of materials throughout a variety of experimental probes using the same batch with large crystals. We believe that these "standard dataset" should contribute to bridging the future application as a properly establishing the magnetic refrigerant.

Appendix A

In Figure A1, we present the specific heat as a function of the temperature of the stoichiometric $HoAl_2$ and Al-deficiency $HoAl_{1.97}$ crystals. The sample dependence shows that the aluminum deficiency suppresses the ferromagnetic transition temperature at T_C, whereas it has little effect on the spin reorientation temperature at T_{SR}. Additionally, we can see that the peak height is suppressed, and the peak width becomes broadened at T_{SR} for the Al deficiency sample, although we need to be careful to evaluate the specific heat with the first-ordered phase transition when the relaxation method is applied for the measurements.
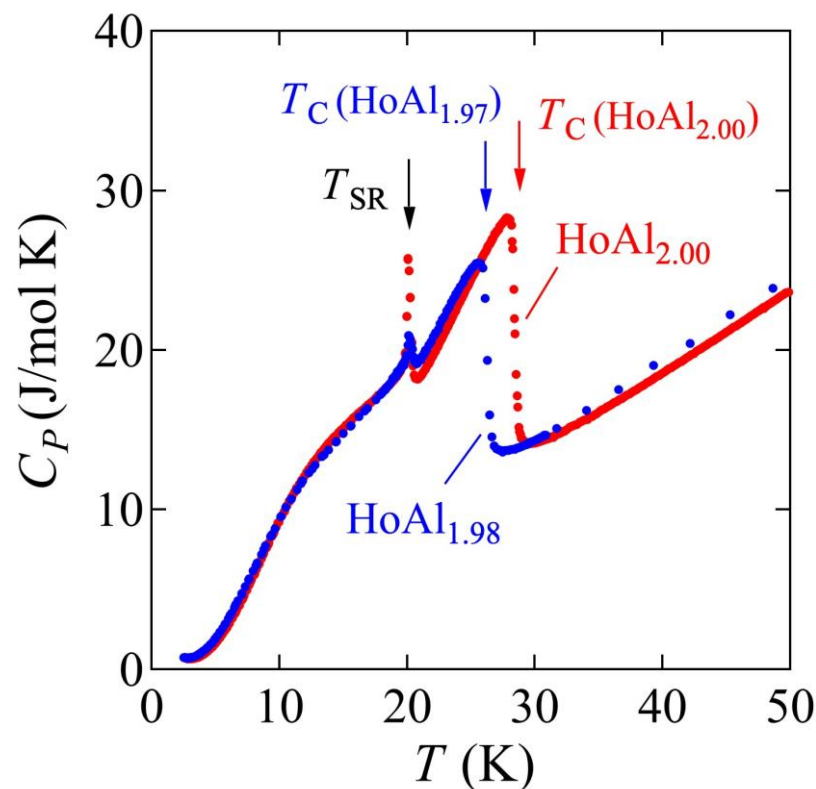
Figure A1. Temperature dependence of specific heat (C_P) of the stoichiometric HoAl$_2$ and Al-deficiency HoAl$_{1.97}$ crystals.

References

1. Tishin, A.M. Magnetocaloric Effect: From Theory to Practice. In *Encyclopedia of Materials: Science and Technology*; Buschow, K.H.J., Cahn, R.W., Flemings, M.C., Ilschner, B., Kramer, E.J., Mahajan, S., Veyssière, P., Eds.; Elsevier: Oxford, UK, 2001; pp. 5035–5041. [CrossRef]
2. Pecharsky, V.K.; Gschneidner, K.A. Magnetocaloric Effect from Indirect Measurements: Magnetization and Heat Capacity. *J. Appl. Phys.* **1999**, *86*, 565. [CrossRef]
3. Gschneidner, K.A. The Magnetocaloric Effect, Magnetic Refrigeration and Ductile Intermetallic Compounds. *Acta Mater.* **2009**, *57*, 18. [CrossRef]
4. Gschneidner, K.A.; Pecharsky, V.K. Magnetocaloric Materials. *Annu. Rev. Mater. Sci.* **2000**, *30*, 387. [CrossRef]
5. Zhu, Y.; Asamoto, K.; Nishimura, Y.; Kouen, T.; Abe, S.; Matsumoto, K.; Numazawa, T. Magnetocaloric Effect of (Er$_x$R$_{1-x}$)Co$_2$ (R = Ho, Dy) for Magnetic Refrigeration between 20 and 80K. *Cryogenics* **2011**, *51*, 494. [CrossRef]
6. Zhang, H.; Gimaev, R.; Kovalev, B.; Kamilov, K.; Zverev, V.; Tishin, A. Review on the Materials and Devices for Magnetic Refrigeration in the Temperature Range of Nitrogen and Hydrogen Liquefaction. *Phys. B Condens. Matter* **2019**, *558*, 65. [CrossRef]
7. Kamiya, K.; Matsumoto, K.; Numazawa, T.; Masuyama, S.; Takeya, H.; Saito, A.T.; Kumazawa, N.; Futatsuka, K.; Matsunaga, K.; Shirai, T.; et al. Active Magnetic Regenerative Refrigeration Using Superconducting Solenoid for Hydrogen Liquefaction. *Appl. Phys. Express* **2022**, *15*, 053001. [CrossRef]
8. Oesterreicher, H. Structural, Magnetic and Neutron Diffraction Studies on TbFe$_2$-TbAl$_2$, TbCo$_2$-TbAl$_2$ and HoCo$_2$-HoAl$_2$. *J. Phys. Chem. Solids* **1973**, *34*, 1267. [CrossRef]
9. Williams, C.M.; Koon, N.C.; Das, B.N. Spin Reorientations in Single Crystal HoAl$_2$. *J. Appl. Phys.* **1979**, *50*, 1669. [CrossRef]
10. Yamamoto, T.D.; Takeya, H.; Saito, A.T.; Terashima, K.; Numazawa, T.; Takano, Y. Magnetocaloric Particles of the Laves Phase Compound HoAl$_2$ Prepared by Electrode Induction Melting Gas Atomization. *J. Magn. Magn. Mater.* **2022**, *547*, 168906. [CrossRef]
11. Numazawa, T.; Kamiya, K.; Utaki, T.; Matsumoto, K. Magnetic Refrigerator for Hydrogen Liquefaction. *Cryogenics* **2014**, *62*, 185. [CrossRef]
12. Barbara, B.; Rossignol, M.F.; Boucherle, J.X. Magnetic Behavior of HoAl$_2$ Single Crystal. *Phys. Lett. A* **1975**, *55*, 321. [CrossRef]
13. Ibarra, M.R.; Lee, E.W.; del Moral, A.; Moze, O. Magnetic Anisotropy and Spin-Reorientation in HoAl$_2$. *Solid State Commun.* **1985**, *53*, 183. [CrossRef]
14. Ibarra, M.R.; Moze, O.; Algarabel, P.A.; Arnaudas, J.I.; Abell, J.S.; del Moral, A. Magnetoelastic Behaviour and the Spin-Reorientation Transition in HoAl$_2$. *J. Phys. C Solid State Phys.* **1988**, *21*, 2735. [CrossRef]

15. Patra, M.; Majumdar, S.; Giri, S.; Xiao, Y.; Chatterji, T. Magnetic, Magnetocaloric and Magnetoresistive Properties of Cubic Laves Phase HoAl$_2$ Single Crystal. *J. Phys. Condens. Matter* **2014**, *26*, 046004. [CrossRef] [PubMed]

16. Gil, L.A.; Campoy, J.C.P.; Plaza, E.J.R.; de Souza, M.V. Conventional and Anisotropic Magnetic Entropy Change in HoAl$_2$ Ferromagnetic Compound. *J. Magn. Magn. Mater.* **2016**, *409*, 45. [CrossRef]

17. Pistawala, N.; Rout, D.; Saurabh, K.; Bag, R.; Karmakar, K.; Harnagea, L.; Singh, S. Crystal Growth of Quantum Materials: A Review of Selective Materials and Techniques. *Bull. Mater. Sci.* **2021**, *45*, 10. [CrossRef]

18. Ito, T.; Ushiyama, T.; Yanagisawa, Y.; Tomioka, Y.; Shindo, I.; Yanase, A. Laser-Diode-Heated Floating Zone (LDFZ) Method Appropriate to Crystal Growth of Incongruently Melting Materials. *J. Cryst. Growth* **2013**, *363*, 264. [CrossRef]

19. Kaneko, Y.; Tokura, Y. Floating Zone Furnace Equipped with a High Power Laser of 1 KW Composed of Five Smart Beams. *J. Cryst. Growth* **2020**, *533*, 125435. [CrossRef]

20. Kikugawa, N.; Terashima, T.; Kato, T.; Hayashi, M.; Yamaguchi, H.; Uji, S. Bulk Physical Properties of a Magnetic Weyl Semimetal Candidate NdAlGe Grown by a Laser Floating-Zone Method. *Inorganics* **2023**, *11*, 20. [CrossRef]

21. Nagai, I.; Shirakawa, N.; Ikeda, S.-I.; Iwasaki, R.; Nishimura, H.; Kosaka, M. Highest Conductivity Oxide SrMoO$_3$ Grown by a Floating-Zone Method under Ultralow Oxygen Partial Pressure. *Appl. Phys. Lett.* **2005**, *87*, 024105. [CrossRef]

22. Bobowski, J.S.; Kikugawa, N.; Miyoshi, T.; Suwa, H.; Xu, H.-S.; Yonezawa, S.; Sokolov, D.A.; Mackenzie, A.P.; Maeno, Y. Improved Single-Crystal Growth of Sr$_2$RuO$_4$. *Condens. Matter* **2019**, *4*, 6. [CrossRef]

23. Martien, D.; Williamsen, M.; Spagna, S.; Black, R.; DaPron, T.; Hogan, T.; Snow, D. An Ultrasensitive Differential Capacitive Dilatometer. *IEEE Trans. Magn.* **2019**, *55*, 1. [CrossRef]

24. Pourarian, F. Exchange-Striction of Rare Earth-Al$_2$ Laves Phase Compounds. *J. Phys. Chem. Solids* **1980**, *41*, 123. [CrossRef]

25. Baran, S.; Duraj, R.; Szytuła, A. Magnetocaloric Effect and Transition Order in HoAl$_2$. *Acta Phys. Pol. A* **2015**, *127*, 815. [CrossRef]

26. Maeno, Y.; Ando, T.; Mori, Y.; Ohmichi, E.; Ikeda, S.; NishiZaki, S.; Nakatsuji, S. Enhancement of Superconductivity of Sr$_2$RuO$_4$ to 3 K by Embedded Metallic Microdomains. *Phys. Rev. Lett.* **1998**, *81*, 3765. [CrossRef]

27. Shoenberg, D. *Magnetic Oscillations in Metals*; Cambridge University Press: Cambridge, UK, 2009; ISBN 9781316583173.